Microfluidic Device for Single-Molecule Experiments with Enhanced Photostability

Edward A. Lemke[†‡§], Yann Gambin[†], Virginia Vandelinder[#], Eric M. Brustad[‡], Hsiao-Wei Liu[†], Peter G. Schultz[‡], Alexander Groisman[*#] and Ashok A. Deniz[†*]

Department of Molecular Biology, Department of Chemistry, The Scripps Research Institute, 10550 N Torrey Pines Rd and Department of Physics, University of San Diego California, 9500 Gilman Dr., La Jolla, CA 92037

Supplementary Material

Design of the microfluidic device. The microfluidic device was designed to deoxygenate solutions in the microchannels and achieve an oxygen-free environment in the optical interrogation region where the FRET measurements are performed (**Fig. 1 and Supplementary Fig. 1**). The deoxygenation occurred by molecular diffusion of oxygen (O_2) from the solutions in the flow channels through porous PDMS walls to nearby gas channels that were continuously ventilated with pure nitrogen (N_2). Unlike some previous designs, where microfluidic devices were made of two layers of PDMS and had two layers of microchannels, with gas channels positioned on top of flow channels[1,2], the microfluidic devices used in the present study were made of a single cast of PDMS, with gas channels flanking the flow channels. The single-layer design substantially simplified the fabrication procedure, making it possible to produce microfluidic devices at a low labor cost and making the devices more durable and reusable.

In addition to achieving maximal deoxygenation, the dimensions and layout of the flow channels were chosen to provide optimized conditions for single molecule FRET spectroscopy in the measurement channel and fast and efficient buffer exchange in a laminar sheath flow immediately upstream of the measurement region. The choice of an 80 μm flow channel depth was dictated by the relatively high levels of autofluorescence, as compared to water, of the cover glass at the bottom and PDMS chip at the top. This autofluorescence could contribute to the FRET background, thus reducing data quality. The channel depth of 80 μm enabled positioning of the confocal detection region for single molecule measurements at a distance of 40 μm from both glass and PDMS, making it possible to optimize the detection sensitivity without an appreciable increase in the fluorescence background. The width of the measurement channel was fixed at 300 μm such that the beams focused and collected by the high-NA objective used in the experiments (40x/1.2NA water immersion) would not be distorted by passing

through the PDMS side walls of the channel, which had a refractive index of ~1.41 as compared to 1.33 for water.

Buffer exchange was initiated at the 4-channel junction (**Fig. 1 and Supplementary Fig. 1d,2,3**), where the stream of the sample solution was squeezed in a sheath between two streams of buffer coming from two sides. The sample and sheath channels were 30 μm wide at the junction. The sheathed sample stream was directed through a mixing channel to the measurement channel. The mixing channel was 200 μm long and consisted of a 30 μm wide, 50 μm long upstream segment and a 40 μm wide, 150 μm long downstream segment.

The width of the sample solution stream in the 40 μm wide segment, w_p, was 1.8 μm, leading to diffusive exchange between the sample and buffer solutions at a time scale $t_{ex} = w_p^{\,2}/(8D)$. This corresponds to a time scale of ~1 ms for ROXS ($D = 5 \cdot 10^{-6}$ cm^2/s) and ~0.5 ms for the denaturant (GdmCl, $D = 10^{-5}$ cm^2/s). In the experiments reported in the paper, the flow velocity through the confocal volume was 0.9 mm/s, corresponding to the sample flow velocity of 6.8 mm/s in the 40 μm wide segment of the mixing channel with a time of ~200 μm/6.8 mm/s = 29 ms (~68$\cdot t_{ex}$ for the denaturant) available for the buffer exchange. Numerical simulations (**Supplementary Fig. 2-4**) indicated that before the sample arrives at the measurement channel, the concentration of denaturant in the sample is reduced by 92% compared with its original value, and the concentration of ROXS reaches 90% of its value in the sheath buffer.

The time required for protein molecules in the sheathed sample stream to reach the side walls of the mixing channel by diffusion can be estimated as $t_{side} = w_m^{\,2}/(8D_{pr}) \approx 2$ s, where $w_m = 40$ μm is the width of the mixing channel and the diffusion coefficient of the protein molecules is conservatively estimated as $D_{pr} = 10^{-6}$ cm^2/s. Because $t_{side} >> 29$ ms, protein molecules were not expected to interact with the side walls. For protein molecules moving near the mid-plane of the channel, the transit time between the entrance of the mixing channel and the confocal volume (150 μm from the end of the 40 μm wide mixing channel) was estimated as ~130 ms, corresponding to a diffusion distance of ~5.5 μm. This diffusion distance was substantially less than the 40 μm distances from the mid-plane to the top and bottom of the channel, precluding any sample loss due to interactions with the top and bottom channel walls after the buffer exchange.

The microfluidic device (**Fig. 1, Supplementary Fig. 1**) had two buffer inlets for solutions of the oxidizer methyl viologen (MV) and reductant ascorbic acid (AA) that were mixed in the device to produce ROXS,

a mixture found to decrease dye blinking[3]. Whereas each of the two components was independently chemically stable, the ROXS mixture was observed to degrade on a time scale of ~10 min producing a solution with an appreciable autofluorescent background (see also Supplementary Figure 8). We note that a soluble autofluorescent compound is of greater concern for studies on freely diffusing single molecules with a confocal detection geometry (this study) than for studies on immobilized molecules using total internal reflection fluorescence (TIRF) (ref. [3]). Therefore, to prevent the autofluorescence, MV and AA had to be mixed immediately before feeding the buffer with ROXS to the measurement channel. To mix the two components, the microchannels connected to the two buffer inlets merged into a single microchannel with a length $L_m = 62$ mm, and width $w_m = 40$ μm. Because both MV and AA are small molecules with diffusion coefficients $D_{rx} \approx 5 \cdot 10^{-6}$ cm^2/s, the time of mixing by diffusion in the channel was estimated as $t_{rx} = \frac{w_m^2}{D_{rx}} = 3.2$ s. Therefore, the mixing was expected to be complete by the end of the channel, where the mean flow velocity in the channel, $\bar{v}$, was below $L_m / t_{rx} \approx 19$ mm/s, corresponding to a flow velocity of 4.6 mm/s through the confocal volume at the measurement point. In the experiments reported in the paper, the flow velocity through the confocal volume was 1 mm/s, corresponding to $\bar{v} = 4.2$ mm/s in the ROXS mixing channel and suggesting that the mixing of ROXS was complete. The transit time between the entrance of the ROXS mixing channel (where MV and AA first start interacting to form ROXS) and the measurement point, estimated as the sum of the ratios of channel segment lengths to the mean flow velocities within them, was ~42 s, which was substantially less than the degradation time of ROXS (**Supplementary Fig. 1a,c**).

Deoxygenation in the microfluidic device. When designing the device and estimating the deoxygenation, we used values of $D_w = 2 \cdot 10^{-5}$ cm^2/s for O_2 diffusivity in water, 1.3 mM for O_2 solubility in water at 25 °C at an O_2 partial pressure of 1 atm (pure oxygen), and 0.18 for O_2 solubility in PDMS (the ratio between the concentration of O_2 in a piece of PDMS and in the atmosphere around it at equilibrium) [4]. This solubility corresponds to a concentration of oxygen, [O_2], in PDMS of 0.18/22.4 M = 8.04 mM when PDMS is saturated with pure O_2 at 1 atm, and ~6 times higher solubility of O_2 in PDMS as compared with water. Therefore, according to Henry's law, [O_2] in a PDMS wall of a channel was expected to be ~6 times higher than in an aqueous solution inside the channel. The diffusivity of O_2 in PDMS was taken to be $D_p = 1.3 \cdot 10^{-5}$ cm^2/s, as measured in our previous study [2]. We deliberately used this conservative estimate, because a higher value of the diffusivity, $3.4 \cdot 10^{-5}$ cm^2/s, as reported in the literature [4], would result in improved operation of the device.

The concentration of oxygen ($[O_2]$) in the flow channels at steady state (constant flow rate in all channels) is defined by three competing processes: lateral diffusion of $[O_2]$ from the flow channels into the gas channels, vertical diffusion of $[O_2]$ from the atmosphere and from the porous PDMS chip (which is initially saturated with air) into the flow channels and advection due to the flow of the solutions (which are saturated with air when fed into the device). To account for these processes in the device design, we used a combination of analytical estimates and simplified numerical simulations made using FemLab (Comsol, Palo Alta, CA). First, we performed two-dimensional (2D) simulations of $[O_2]$ in a cross-section of the device ignoring the flow of liquids through the microchannels. The device was represented by a 5 mm thick and 10 mm wide PDMS chip with a gas-impermeable lower boundary, corresponding to the cover glass, and with $[O_2]$ = 21% at the top and on the sides. Two gas channels ventilated with N_2 at the bottom of the device were represented by two rectangular protrusions with areas identical to the gas channel cross-sections and with $[O_2]$ = 0 at the boundaries of the protrusions (**Supplementary Fig. 5**). Since the simulation software did not have an option to account for the ~6-fold jump in $[O_2]$ at the boundaries of the flow channels, a flow channel between the gas channels was represented by a rectangular region at the bottom between the gas channels with material properties identical to those of PDMS (**Supplementary Fig. 5b**).

As a representative $[O_2]$ in the flow channel, we took its value in the middle between the gas channels at 40 μm from the bottom, corresponding to the longitudinal axis of symmetry of the flow channel. Simulations of steady-state distributions of $[O_2]$ indicated that, as expected, low values of $[O_2]$ in the flow channel are achieved when the gas channels are wide and deep and when the distance between them is small. Based on the results of the simulations, we chose to use gas channels 160 μm deep and 200 μm wide, with a 240 μm spacing between them and a 40 μm wide flow channel. With a 100 μm distance between the gas and flow channels, this configuration made it possible to use a relatively simple and robust fabrication procedure with easy alignment between the 80 μm and 160 μm tall patterns on the master mold. In addition, the 100 μm distance between the channels ensured reliable reversible bonding of the PDMS chips to the cover glass. The steady-state simulation of $[O_2]$ distribution predicted a $[O_2]$ of ~0.3% in the flow channel, corresponding to a 70 fold reduction compared with an air-saturated aqueous solution. A more refined simulation, taking into account the fact that the gas channels in the device were folded into serpentine lines with a considerable footprint, (**Supplementary Fig.** 1b) predicted an $[O_2]$ of <0.2% (**Fig. 1c, Supplementary Fig. 5c,d)** corresponding to >100-fold reduction.

Because of the relatively large thickness of the chip and the relatively low diffusivity of O_2 in PDMS, the steady-state distribution shown in **Supplementary Fig. 5c,d** would require considerable time to reach. To simulate the transition to the steady state, we performed a time dependent simulation of [O_2] in the same computational domain as in **Supplementary Fig. 5c,d**, with the same boundary conditions and with [O_2] = 21% everywhere in the beginning, corresponding to a PDMS chip saturated with air. The simulation predicted that [O_2] in the flow channel is reduced to <0.25% within 10 min from the start of the flow of N_2 through the gas channels. This result of the simulation suggested that to achieve low levels of [O_2] in the flow channels, the PDMS chip needs to be first deoxygenated by ventilating the gas channels with N_2 for >10 min. (We note that the PDMS deoxygenation time is 2.7 times lower if the diffusivity of [O_2] is $3.4 \cdot 10^{-5}$ cm^2/s as reported in the literature[4].)

To evaluate the effect of advection of O_2 by the flow of a sample solution and buffers through the flow channels, we considered one-dimensional horizontal diffusion across the channels. When new boundary conditions are imposed on the two side walls of a flow channel with the width $w_{ch} = 40$ μm (corresponding to a stream of an aerated buffer solution reaching the region where the flow channel is flanked by two gas channels; **Fig. 1a**), [O_2] in the flow channel is homogenized within time $\tau_{ch} = w_{ch}^2/(8D_w) \approx 0.1$ s. If [O_2] in the flow channel can be considered as uniform, the deoxygenation of the solution in the flow channel by diffusion through its two PDMS walls, each with the thickness $d = 100$ μm, towards the two gas channels has the dynamics of an exponent decaying with a characteristic time $\tau_{wall} = dw_{ch}/(2 \cdot 6 \cdot D_p) \approx 0.25$ s, where the factors of 2 and 6 are due to two side walls and 6-times difference in [O_2] in absolute units between the solution in the channel and the PDMS wall. These estimates indicate that the time-limiting step in the solution deoxygenation is the diffusion of O_2 through the channel walls rather than homogenization of [O_2] inside the flow channel. Therefore, the time required for a ~100-fold reduction of [O_2] from 21% in the solution fed to the device to the limiting value of 0.2%, as predicted by the steady-state 2D simulation (**Supplementary Fig. 5c,d**), can be estimated as $\tau_{deox} = \tau_{wall} \ln(100) \approx 1.2$ s.

Hence, for complete deoxygenation of the solution, the length of the segment of the flow channel where it is flanked by gas channel, L, should be $L > \tau_{deox}\bar{v}$, where $\bar{v}$ is the mean velocity of the solution flow. For the two sheath buffer flow channels of the microfluidic device (**Fig. 1a, Supplementary Fig. 1a,c**), the length of the deoxygenation segments was L = 27 mm, allowing for a maximal value of $\bar{v}$ of ~22 mm/s. The actual value of $\bar{v}$ in the buffer channels was normally ~2.5 mm/s (corresponding to flow velocities of 0.9 mm/s through the confocal volume at the measurement point in

the 300 μm wide test region). Therefore, by the time of arrival at the point of merging with the sample flow at the 4-channel junction, $[O_2]$ in the buffer channels was expected to reach a steady-state value defined by the diffusion through PDMS and independent of the flow of the buffer. The length of the deoxygenation segment of the channel with the sample solution was 3.5 mm (**Supplementary Fig. 1a**), and because of the >10 times lower value of $\bar{v}$ in this channel, the deoxygenation in the sample channel was always more thorough than that in the sheath buffer channels. The measurement point was located in the middle of the 300 μm wide measurement channel, where the distance between the gas channels was 500 μm. A steady-state 2D simulation for such channel layout predicted $[O_2]$ = 1.1%. Nevertheless, the distance between the exit of the 40 μm wide mixing channel and the measurement point was only 150 μm, corresponding to a passage time of $t_{pas} =$ 100 ms for the experimental flow velocity, as obtained from flow simulations with FemLab at 0.9 mm/s velocity in the confocal volume. This passage time was substantially shorter than the O_2 diffusion time along the vertical direction of the channel (the direction of flow of O_2 from the PDMS chip) estimated as $\tau_{vert} = h^2/(8D_w) \approx 400$ ms. Therefore, $[O_2]$ in the confocal volume at the measurement point was expected to be $0.2\% + (1.1\% - 0.2\%)[1 - \exp(-t_{pas}/\tau_{vert})] \approx 0.4\%$, twice higher than in the 40 μm channels, but ~50 fold lower than in an air-saturated solution.

Fabrication of the microfluidic device:

The microfluidic device consisted of a PDMS chip sealed by a #1 cover glass. The chip was cast out of PDMS (10:1 mixture of parts A and B of Sylgard 184 by Dow Corning, Midland, MI) using a master mold fabricated in a two-step photolithography process described in detail elsewhere[5]. Briefly, a 5 in. silicon wafer was spin-coated with a 80 μm layer of a UV-curable epoxy (SU8-2050 by Microchem), exposed to UV-light through a photomask (transparency photoplotted at 25,000 dpi), baked to cure the UV-treated PDMS, spin-coated with another 80 μm layer of the epoxy, exposed through a second photomask, baked, and developed. The pattern of cured SU8 on the completed master mold had features of two heights, 80 μm (for flow channels) and 160 μm tall (for gas channels). To make the PDMS chip, a 5 mm thick layer of PDMS pre-polymer was poured onto the mold and then baked in an 80 °C oven for ~40 min to cure PDMS. The PDMS was then peeled off the wafer, trimmed to the size for individual chips, and holes were punched in the chips to produce inlet and outlet ports. The PDMS chips were reversibly bonded to cover glasses by overnight baking at 80 °C.

Microfluidic setup: flow control and robustness of operation.

The solutions fed to the inlets and drawn off from the outlet were kept in modified 500 μL eppendorf tubes sealed with PDMS plugs. Each plug had two small holes punched in it using a gauge 20 luer stub. To connect the solution in a tube to an inlet (or outlet), a segment of #30 AWG Thin Wall PTFE tubing (Cole Parmer Instrument Company; Vernon Hills, Illinois) was pushed through one of the holes to a position close to the bottom of the tube, and the other end of the segment was inserted into the inlet (or outlet). A luer stub was inserted into another hole in the plug, making it possible to drive the flow through the device by pressurizing the air in tubes connected to the inlets. The small eppendorf tubes and the narrow PTFE tubing (inner diameter of 0.25 mm; internal volume of 1 μL per 20 mm length) made it possible to perform experiments with small amounts of sample and buffers and to use the sample and buffers down to the last ~20 μL. The solutions in the eppendorf tubes were centrifuged prior to use to prevent occasional contamination particles and debris from entering the tubing. In addition, the solutions could easily be examined for bubbles.

The pressure of compressed air supplied to the eppendorf tubes was controlled at a resolution of ~10 Pa using two pressure regulators (#8286 by Porter Instruments, Hatfield, Pennsylvania, USA 0 – 2.5 psi) and measured with an accuracy of ~20 Pa with an electronic gauge (Heise, Stratford, CT). For all three inlets, nearly the entire pressure drop between the inlet and outlet occurred upstream of the 4-channel

junction, where the sample and sheath streams merged. Therefore, the volumetric flow rates of the sample and buffer were proportional to pressures at the respective inlets. The hydrodynamic resistance of the channel line connecting the sample inlet with the 4-channel junction was only ~1.5 times higher than the resistance of the lines between the buffer inlets and the junction. Therefore, to obtain a narrow sample stream for rapid buffer exchange, the sample inlet pressure had to be set substantially lower than the buffer inlet pressure. In the experiments described in the paper, the buffer inlets were both pressurized at 4 kPa and the sample inlet was pressurized at 0.5 kPa with respect to the outlet.

Flow velocities in various channels were measured by analyzing streak lines produced by 2 μm fluorescent beads (Bangs Laboratories, Fishers, IN). The extent of the longest streak line divided by the exposure time was taken as the maximum velocity in the channel, and the values of the mean flow velocity, $\bar{v}$, and volumetric flow rate, Q, were calculated based on the channel cross-section using the equations for developed laminar flow in rectangular channels. The values of Q were 0.36 μL/min for each of the buffer inlets (a total buffer flow of 0.72 μL/min) and 0.052 μL/min for the sample inlet, corresponding to a sample stream width of 1.8 μm in the 40 μm wide mixing channel. In the 300 mm wide measurement channel, the sample stream width was ~20 μm, making it easy to align the confocal detection volume with the stream. The flow velocity at the location of the confocal volume in the measurement region was measured at 0.9 mm/s with an uncertainty of ~5%.

Because of the large ratio of the volumetric flow rate of the buffer to that of the sample, the flow velocity through the confocal volume was nearly entirely defined by the pressure at the buffer inlets (being proportional to it) and almost independent of the sample inlet pressure. Given the 10 Pa sensitivity of the pressure regulator, the flow velocity and the passage time through the confocal volume were adjustable with ~0.25% precision. The adjustment of the flow velocity could be used in combination with tuning of the FRET microscopy system for optimal sample interrogation. A change in the buffer inlet pressure by, say, a factor of 1.5 would change the flow velocity by about the same factor, thus substantially modifying the conditions for optical interrogation of the sample. The 1.5-fold pressure variation would also change the width of the sample stream and the time available for buffer exchange in the mixing channel. However numerical simulations (not shown; cf. **Supplementary Fig. 2-3**) indicated that the concentration of the denaturant at the measurement point would only change by ~2% (with 100% being its original concentration in the sample), which would likely have little effect on the protein conformation. Furthermore, because of the excessive time available for deoxygenation upstream of the 4-channel junction and relatively small (~0.2%) increase in $[O_2]$ on the way from the mixing channel to the measurement point, the 1.5-fold change in the buffer inlet pressure would only

cause ~0.1% change in [O_2] in the confocal volume and would likely have no measurable effect on the FRET signal.

The sample inlet pressure controlled the width of the sample stream and had almost no effect on the flow velocity. Therefore, the sample stream width was adjustable with ~2% precision (10 Pa in pressure), and a 1.5-fold variation in the sample inlet pressure would cause a nearly proportional variation of the sample stream width, leading to <3% change in the concentration of the denaturant at the measurement point, without any other substantial changes in the setup operation. According to numerical simulations (not shown), the removal of the denaturant could be made as complete as ~96% by reducing the sample inlet pressure to 0.25 kPa (with the sample stream width at a sufficiently large value of 8 μm in the measurement channel). These arguments show that the setup can be accurately tuned for best performance and, at the same time, its basic operation does not require fine adjustment of inlet pressures, being perturbed relatively little even when the inlet pressures change as much as 1.5-fold. The relatively short transit time of the sample solution between the point where the buffer exchange begins and the measurement point (~100 ms for the experiments reported in this work) suggests that the setup can be used for studies of protein folding kinetics on a 100 ms scale (**Supplementary Fig.4**).

Measurements of oxygen concentration in microchannels.

The concentration of oxygen, [O_2], in the flow channels was measured using a solution of the oxygen-sensitive fluorescent dye ruthenium tris(2,2'-dipyridyl) dichloride hexahydrate (RTDP, 0.5 g/l in PBS, Ambion, Austin, TX)[6,7]. The fluorescence of RTDP is quenched by oxygen, with the intensity of fluorescence, I, decreasing with increasing [O_2] according to the Stern-Volmer equation, $I_0 / I = 1 + K_q[\mathrm{O}_2]$, where I_0 is the intensity of fluorescence without oxygen, and K_q is the quenching constant. It is convenient to measure [O_2] as a percentage of its value in water saturated with pure oxygen at 1 atm, so that [O_2] in water saturated with air is 21%. The value of K_q corresponding to this definition of [O_2] is dimensionless, but depends on the temperature and ionic content of the solution, and therefore has to be determined experimentally.

Measurements of RTDP fluorescence were performed on a Nikon TE300 inverted fluorescence microscope (Nikon, Melville, NY). The source of illumination was a blue LED (Royal Blue Luxeon V by Lumileds, San Jose, CA; 700 mW with central wavelength 455 nm) mounted on a cooling fan and inserted into a modified Nikon lamp house. The LED was powered by a regulated DC supply and

provided stable illumination with <0.5% variation of intensity over several hours. Images were taken with an Olympus 20×/0.7 WI objective and a Coolsnap HQ camera (Photometrics, California). We first used the microscope to evaluate K_q by measuring the intensity of fluorescence of the RTDP solution, I, in a 100 μm deep and 300 μm wide microchannel, when the solution was saturated with N_2, air, and O_2 ($[O_2]$ = 0, 21%, and 100%, respectively) using a technique described elsewhere [2]. Based on the three fluorescence intensities, I_0, $I\ (21\%)$, and $I\ (100\%)$, K_q was estimated to be 2.25 (per 100%) with a relative uncertainty of ~0.5%. Next, all three inlets of the microfluidic device were fed with the RTDP solution by applying a pressure of 4 kPa to the buffer inlets and a pressure of 1 kPa to the sample inlet, and creating flow conditions nearly identical to the smFRET experiments reported in the paper. The gas channels were fed with either air or N_2, both at a pressure of 1 psi, the same as in the smFRET experiments. To allow time for equilibration of the gas content in the PDMS chip, fluorescence measurements were started >5 min after the gas supplied to the gas channels was switched from air to N_2 or back. The intensity of RTDP fluorescence when the gas channels were ventilated with air, I_{air}, was measured and the value of I_0 was calculated under the assumption that $[O_2]$ in the flow channels in this case was 21%: $I_0 = I_{air}(1+0.21K_q)$. The gas channels were then ventilated with N_2, the intensity of RTDP fluorescence, I_{N2}, was measured at the point where the FRET measurements where performed, and the value of $[O_2]$ at this point was calculated as $[\text{O}_2] = (I_0 / I_{N2} - 1)/K_q$. In this case the result was indistinguishable from 0 within the 0.5% measurement uncertainty, which was consistent with the estimate of $[O_2]$ ~0.4% obtained from the numerical simulations for gas channels ventilated with N_2.

DNA and Protein Sample preparation:

Two complementary strands of DNA were labeled using standard succinimide chemistry as described in the manufacturers' kits (Invitrogen, Carlsbad, CA and GE Healthcare, Piscataway, NJ). The following sequences (obtained from Integrated DNA Technologies, San Diego, CA) were utilized to place the two dyes 9 bases apart:

5'-CTC TTC AGT(A488) TCA CAG TCC ATC CTA TCA GC-3'

5'-GCT GAT AGG ATG GAC TGT GAA CTG AAG AG-3' Cy5

Alexa488 (Donor, D) was attached by reaction of its N-hydroxysuccinimidyl ester with an amino group introduced at T9 (via a C6 Amino Modifier dT), and Cy5 or Alexa647 (Acceptor, A) was attached to the 3′ terminus of the complementary strand by reaction of its N-hydroxysuccinimidyl ester with a 3′-amino group. Labeled DNA strands were purified by polyacrylamide gel electrophoresis. The duplex construct

was prepared by annealing the purified complementary labeled DNA strands prior to use in 2xPBS buffer by heating to 94°C followed by gradual cooling (1°/s) to room temperature.

The NIR dye-pair duplex DNA was prepared in a similar fashion with the same dye-attachment chemistry using Alexa647 as a Donor and Alexa750 as an Acceptor. Strands used for the NIR dye-pair were:
5'-GCT GAT AGG ATG GAC TGT GAA CTG AAG AG -3'- A647
5'-CTC T(A750)TC AGT TCA CAG TCC ATC CTA TCA GC- 3'

Two mutants of the protein T4 lysozyme were expressed, purified, and site-specifically labeled with donor and acceptor dyes at positions 38 and 109 or 5 and 38, as previously reported [8]. Briefly, a cysteine-free variant of bacteriophage T4 lysozyme containing a C-terminal 6Xhistidine sequence (for purification) was genetically modified to introduce a cysteine residue at position 109 and to encode for the unnatural amino acid p-acetylphenylalanine at position 38. The dye Alexa488-hydroxylamine (Invitrogen) was used to label the protein at position 38 by reaction with the introduced ketone, and Cy5-maleimide (GE Healthcare, Piscataway, NJ) was reacted with the cysteine residue at position 109. The same procedure was used to generate another dual-labeled mutant with a cysteine residue at position 5 in addition to the 38TAG mutation. This mutant was labeled with Cy3 at position 5 using standard maleimide coupling and Alexa647 hydroxylamine at position 38 using the orthogonal ligation strategy. Experiments with the dual-labeled protein were performed as described in the text, either in 2xPBS or 2xPBS with 4M guanidinium chloride (GdmCl). The individual components of ROXS, AA and MV, were used as previously described at 1mM each [3].

Single-Molecule FRET and Fluorescence Correlation Spectroscopy Measurements:

Single-molecule FRET experiments were performed as previously described [8]. Briefly, laser light at 488 nm derived from an argon ion laser (Melles Griot, Carlsbad, CA) was coupled into a Zeiss Axiovert 200 microscope (Zeiss, Thornwood, NY) by a single mode fiber (Pointsource, Hamble, UK) and focused into the sample using a Zeiss C-Apochromat 40x, 1.2 NA objective lens, after passing through a $\lambda/4$ plate. The emitted fluorescence light was separated from the excitation light by using a dichroic beam splitter (Q495LP, Chroma Tech. Corp., Rockingham, VT), and further spatially filtered by focusing on a 75 µm pinhole. The filtered emission light was spectrally separated into Donor and Acceptor channels by using another dichroic beam splitter (DC560, Chroma). After passing through bandpass filters [Donor channel, 525/50 (Chroma) and acceptor channel, 700/70 (Chroma)], the light was focused onto and detected by avalanche photon counting modules (SPCM-AQR-14, Perkin-Elmer Optoelectronics, Fremont, CA). For

detection of Cy3 labeled samples the following parts were used instead: Excitation with a 532nm Nd:YAG Laser (Crysta Laser, Reno, NV) and DC532 (Chroma) excitation dichroic, 630 nm dichroic to separate Cy3 and Alexa647 light, and Emission filter 605/40 (Chroma) for detection of Cy3. For the NIR dye pair, excitation was performed with a 633nm Helium-Neon Laser (Melles Griot), and a DC 650 used to separate excitation from emission light. The light was further split into Donor channel (Alexa647) and Acceptor channel (Alexa750) using a DC750 (Chroma) and further filtered using a 700/70 bandpass and a 750 long pass emission filter respectively. A National Instruments counting card and a SPC630 computer card (Becker&Hickl, Berlin, Germany) operating in the FIFO TAG mode were used to record the arrival times of individual photons. Data was analyzed either by binning or by indentifying individual bursts using a previously described burst search algorithm [9]. FRET histogram analysis was carried out on bursts containing more than 40 photon counts (or as given in the text) using IgorPro (Wavemetrics, Lake Oswego, OR). FRET efficiencies (E_{FRET}) were computed from the detected photon counts in the A and D channels (I_A and I_D, corrected for a bleed-through of 2% of fluorescence from the D into the A channel) as proximity factors, $E_{FRET} = \frac{I_A}{I_A + I_D}$, and plotted as histograms of the relative frequencies of occurrence. Gaussian fits to the histograms were calculated by using IgorPro (as displayed in Fig. 2 and Supplementary Fig. 6 and 7) and the peak positions and widths (σ) were obtained from the fitting parameters. The photon signals from the Donor and Acceptor channels were also simultaneously fed into a Hardware correlator (ALV-6010/160; ALV-GmbH, Langen, Germany) to compute the fluorescence cross-correlation function between the two channels. A fast decay component due to blinking from transitions to and from the dark triplet state was clearly visible under some conditions (Supplementary Fig. 6 and 9, and Main Text Fig. 3).

Supplementary Figure 1: (a) – (b) Schematics of the microfluidic device, **(a)** highlighting in blue the network of 80 μm deep flow channels (with the gas channel network in light red), and **(b)** highlighting in red the network of 160 μm deep gas channels (with the flow channel network in light blue). **(c)** Fluorescence micrograph (with some brightfield background) of the region marked by a read box in (a) showing mixing of two liquids, a solution of FITC (fluorescent) and a non-fluorescent buffer, which are fed into the two buffer inlets. The micrograph illustrates how the two components of ROXS, MV and AA, are gradually mixed in a 62 mm long serpentine channel. **(d)** Fluorescence micrograph of the buffer exchange channel (cf. Figure 1c in the main text) from a test when a solution of FITC was fed to the sample inlet and buffer was fed to the two buffer inlets to illustrate the 2D flow focusing of the sample stream (fluorescent stream in the middle) in a sheath flow of the buffer. The sample stream substantially expands after exiting the 40 μm wide buffer exchange channel and entering the 300 μm wide interrogation channel. The FRET measurement point is located at the middle of the lower boundary.

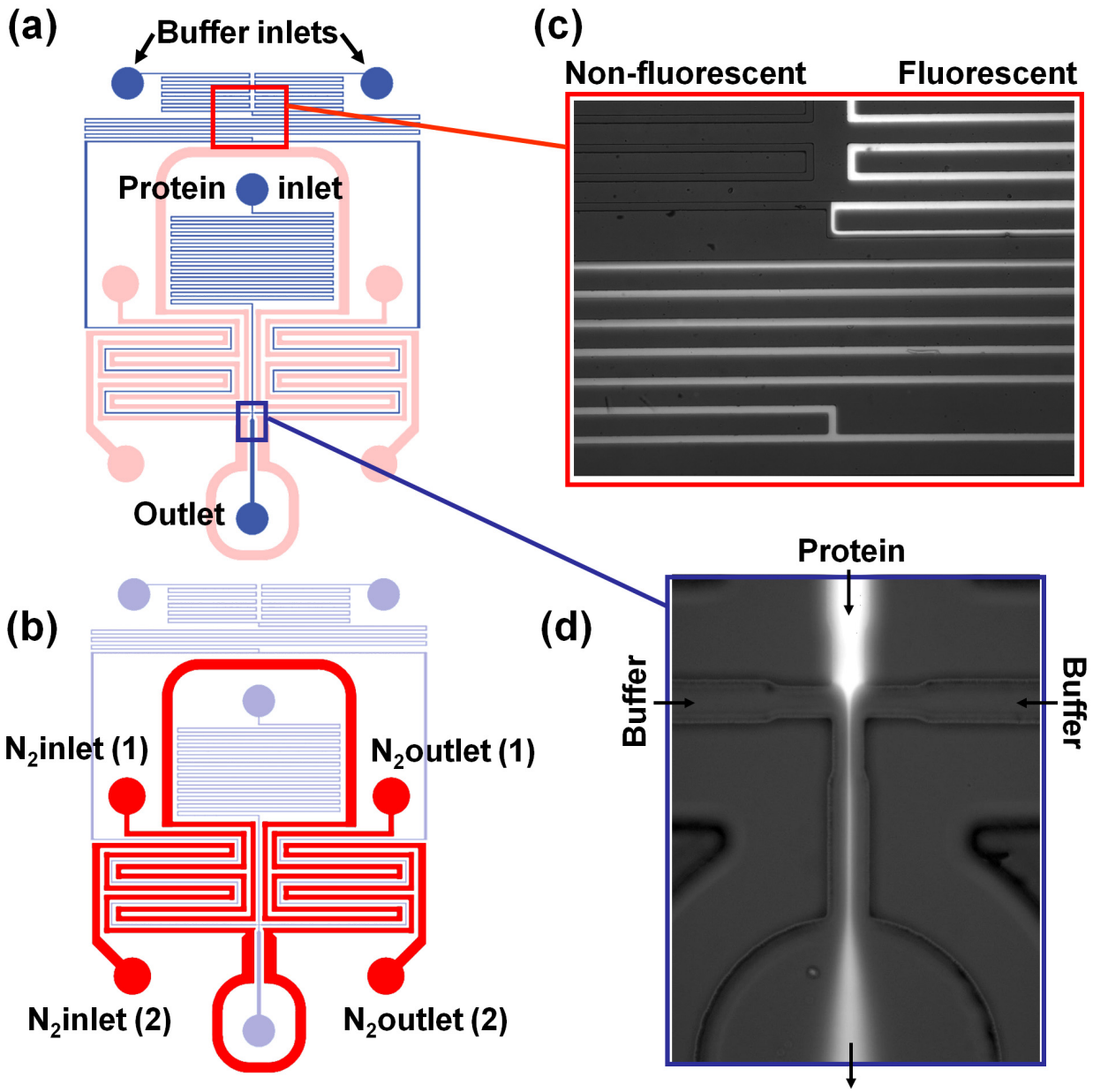

Supplementary Figure 2: **(a)** Distribution of flow velocity in the mid-plane of the functional region of the device from a numerical simulation with FemLab using non-linear Navier-Stokes equation. The simulation was performed to match the conditions of the smFRET experiments: 0.9 mm/s flow speed at the measurement point and 1.8 μm wide sample stream in the 40 μm mixing channel. The measurement point is at x=y=0. **(b)** The time in the flow, t, (in the Lagrangian reference frame of the moving fluid) along the central streamline (y = 0) as a function of the position along the channel, x. The time is computed starting from a reference point, $x0$, near the beginning of the buffer exchange channel, where 10% of the buffer in the sample solution is exchanged (See Supplementary Fig. 3), as $t(x) = \int_{x0}^{x} \frac{dx'}{v(x')}$, where $v(x)$ is the flow velocity as a function x.

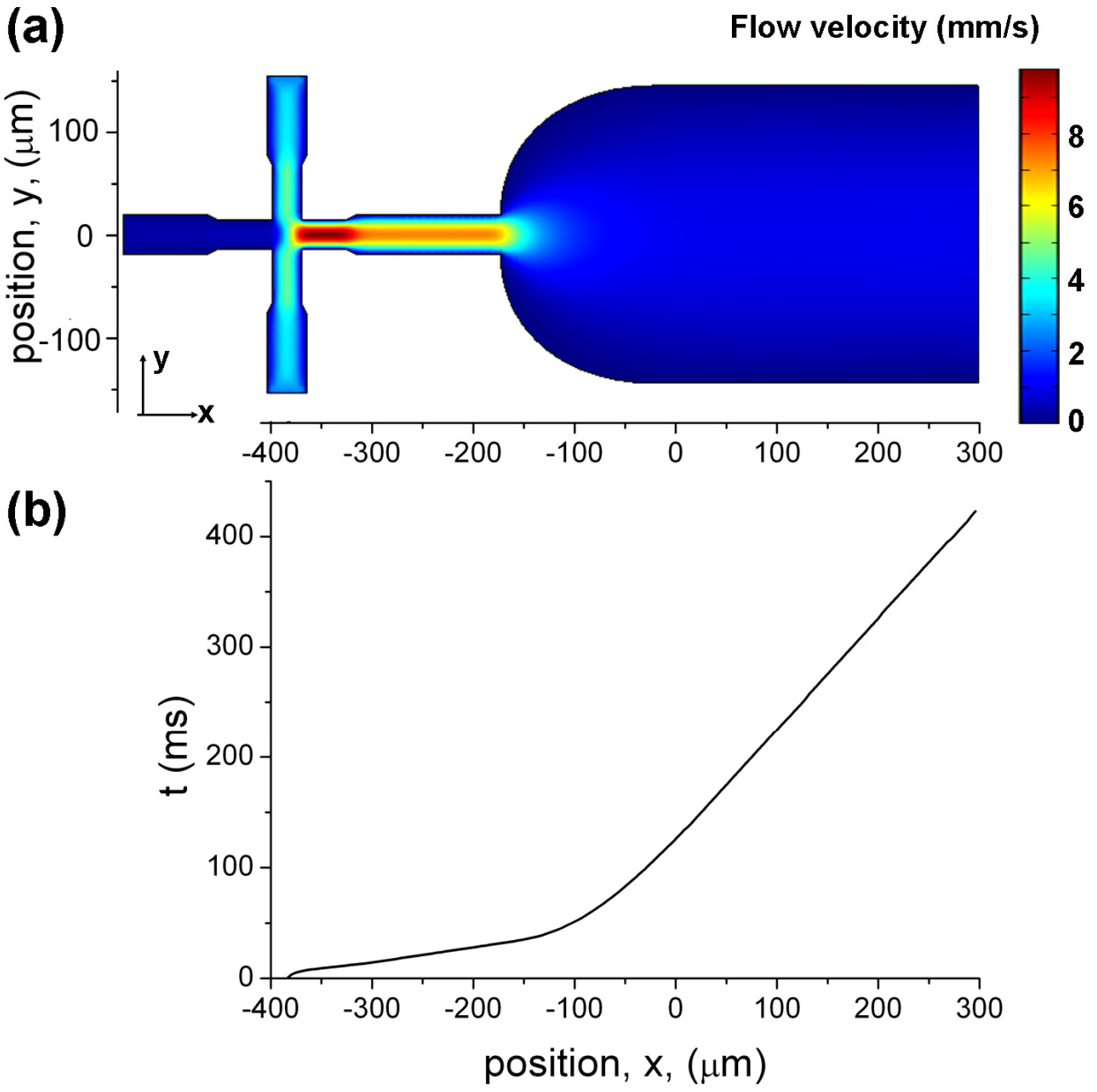

Supplementary Figure 3: (a) Diffusive elution of Guanidinium Chloride (GdmCl) from the sample stream (buffer exchange) as computed numerically using FemLab at the flow conditions of Supplementary Figure 2. Color-coded distribution of GdmCl concentration, c_{Gd}, (legend shown on the right), normalized to its initial value in the sample solution (100%), is shown in the mid-plane of microchannels in the functional region of the device. The coefficient of diffusion of GdmCl molecules is taken at 1×10^{-5} cm^2/s. **(b)** Percentage of buffer exchange in the sample solution (100% - c_{Gd}) along the central streamline (y = 0) as a function of the position, x, in the direction of flow, with x = 0 corresponding to the measurement point.

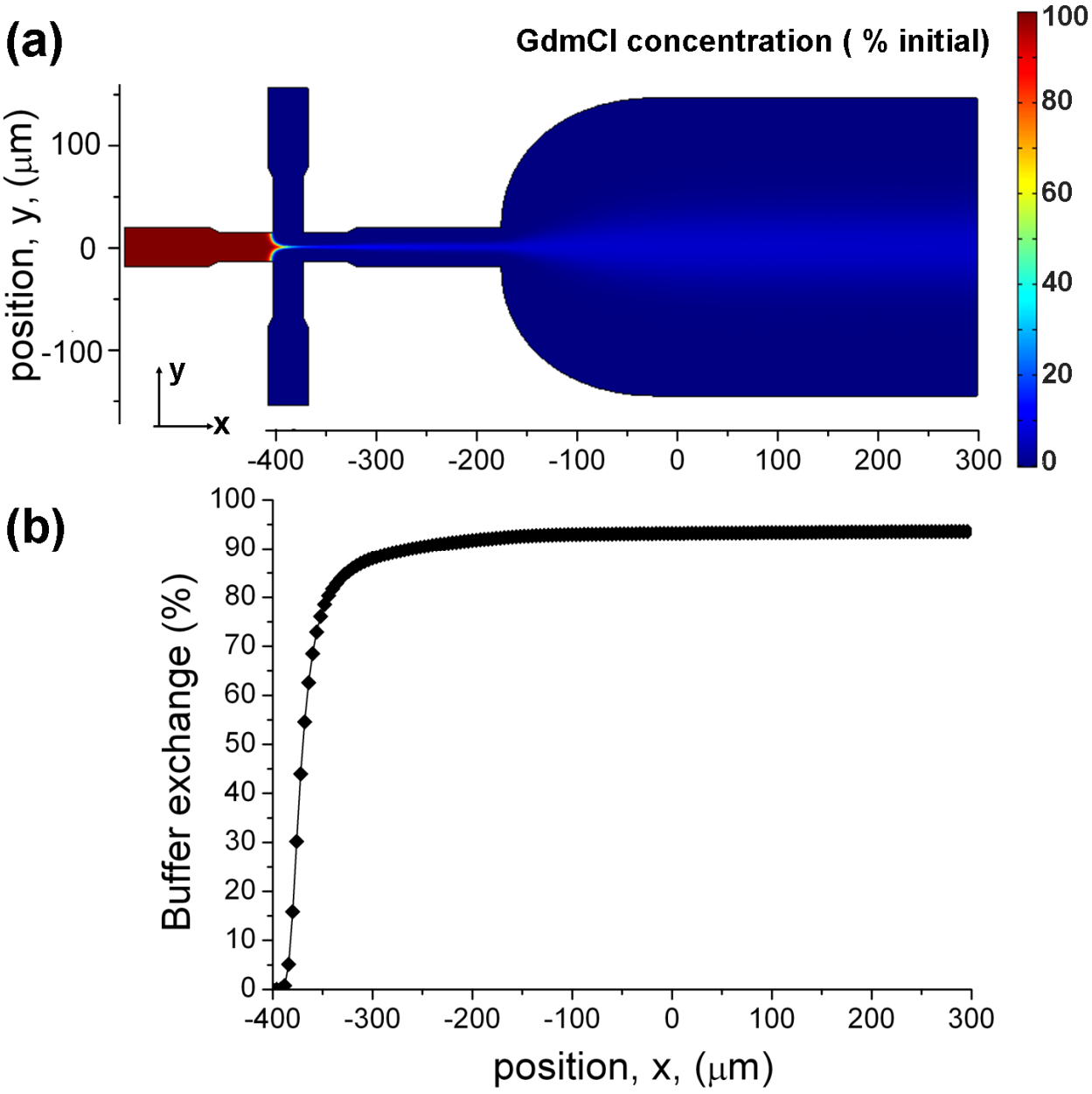

Supplementary Figure 4: Kinetics of the buffer exchange in the sample stream, as calculated from numerical simulations with FemLab. Graph shows percentage of diffusive elution of the denaturant (a molecule with a diffusivity of $1x10^{-5}$ cm^2/s as for GdmCl, which is initially present in the sample solution) as a function of time. The degree of the buffer exchange as a function of time in the flow, t, was evaluated in the middle of the sample stream from the plots of t as a function of the position, x, (Supplementary Figure 2b) and of the buffer exchange as a function of x (Supplementary Fig. 3b). At the measurement point, x = 125 ms.

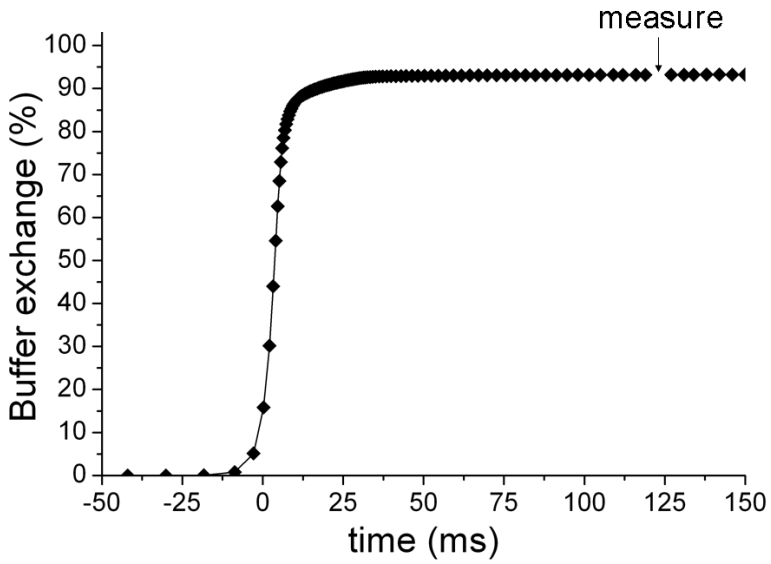

Supplementary Figure 5: Two-dimensional (2D) numerical simulations of the distribution of oxygen concentration, $[O_2]$, in two PDMS chips. Both chips have 10×5 mm cross-sections (horizontal×vertical) with gas-impermeable lower boundaries, corresponding to the cover glass at the bottom of the microfluidic device. $[O_2]$ is equal to 21% at the top and on the sides of the device. The gas channels ventilated with N_2 are represented by 200×160 μm rectangular protrusions at the bottom (identical to the gas channel cross-sections) with $[O_2]$ = 0 at their boundaries. The distributions of $[O_2]$ in the computational domains are color-coded with legends shown on the right. **(a)** Steady-state distribution of $[O_2]$ in a chip with two gas channels separated by 240 μm. **(b)** Magnified view of the region marked by a white dashed box in (a). $[O_2]$ is color-coded from 0 to 0.5%, and areas with $[O_2]$ > 0.5% are blank. Black rectangle in the middle shows the location of a 40×80 μm flow channel. At 40 μm above the bottom in the flow channel, $[O_2]$ = 0.25%. **(c)** Steady-state distribution of $[O_2]$ in a chip with 5 sets of channels, as in the microfluidic device used in the study (Figure 1a in the main text). Each set of channels is identical to the two gas channels with a flow channel in the middle in (a) and (b), and the distance between adjacent sets is 150 μm, as in the actual microfluidic device. **(d)** Magnified view of the region marked by a dashed box in (c) with 3 channel sets. Black rectangles show locations of flow channels. $[O_2]$ is color-coded from 0 to 0.25%, and areas with $[O_2]$ > 0.25% are blank. The levels of $[O_2]$ in flow channels marked by blue, green, and red arrows are 0.17%, 0.11, and 0.10%, respectively. **(e)** $[O_2]$ in the central flow channel [marked by red arrows in (c) and (d)] from a time dependent numerical simulation in the computational domain shown in (c). The initial condition was $[O_2]$ = 21% everywhere.

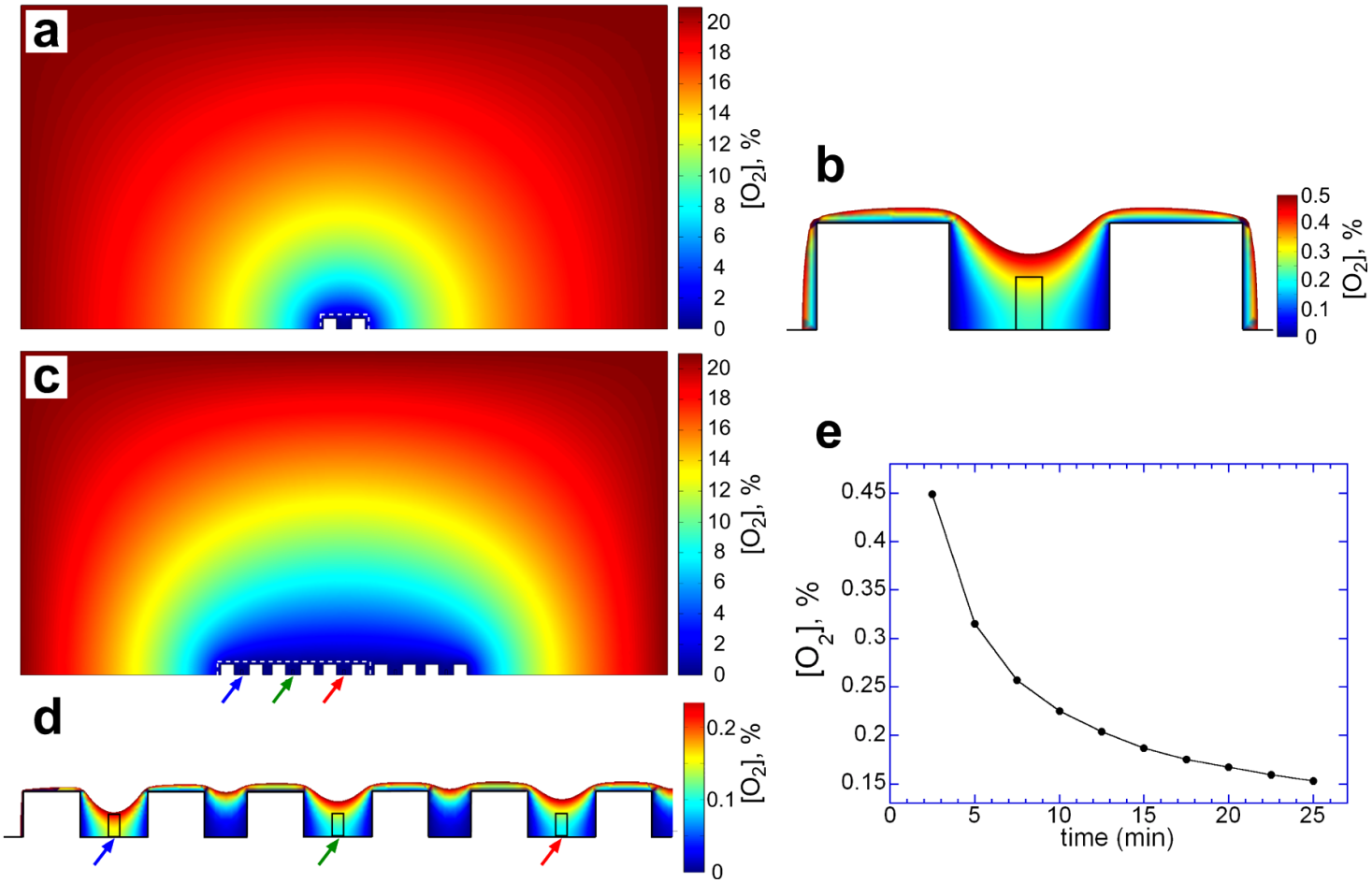

Supplementary Figure 6: Experimental data for FRET and FCS measurements of DNA (Alexa488-Cy5 labeled, analyzed using a burst search algorithm): **(a)** in a cuvette, **(b)** in the microfluidic device with air in the gas channels, **(c)** in the device with deoxygenation by flow of N_2 through the gas channels, and (**d**) in the device with deoxygenation and addition of ROXS. Plots on the left of each panel are FRET histograms; plots in the middle of each panel show the raw photon count data with a binning time of 0.5 ms for D (green) and A (red) channels; plots on the right of each panel show cross-correlation functions, $G(\tau)$. The ratio of areas between the zero and FRET peaks in FRET histograms improves upon changing experimental conditions from the cuvette with no flow in (a) to the microfluidic device with continuous flow through the confocal volume at 1 mm/s in (b). The flow diminishes the zero peak by reducing the photobleaching due to excessively long residence of molecules in the confocal volume and by preventing the re-entry of photobleached molecules into in the confocal volume. On-chip deoxygenation reduces the ratio of the zero peak to the FRET peak by an additional factor of ~3, (c) vs. (b). Fluorescence intensity traces indicate that the deoxygenation reduces the overall intensity of the bursts, (c) vs. (b), which is likely due to enhanced blinking of the dyes. [3,10] A substantial fast fluctuation component is also visible in the correlation function $G(\tau)$ [(c), right panel], as indicated by a curly bracket. This component is suppressed by the addition of ROXS [(d), right panel] with a concurrent increase of the photon counts (brightness) in the burst intensity trace [middle panel in (d) vs. (c)]. The addition of ROXS also reduces the width of the FRET peak, [left panels in (a) vs. (d)], which can be explained by the improved brightness of the dyes as compared with the background. The background originated from autofluorescent species in the buffer (including ROXS) and was particularly pronounced due to relatively high laser power used in all experiments (865 μW at the back aperture of the objective). This setting was chosen to be in a regime in which photostability of dyes was a major limiting factor of the smFRET experiments, and the on-chip deoxygenation was particularly beneficial.

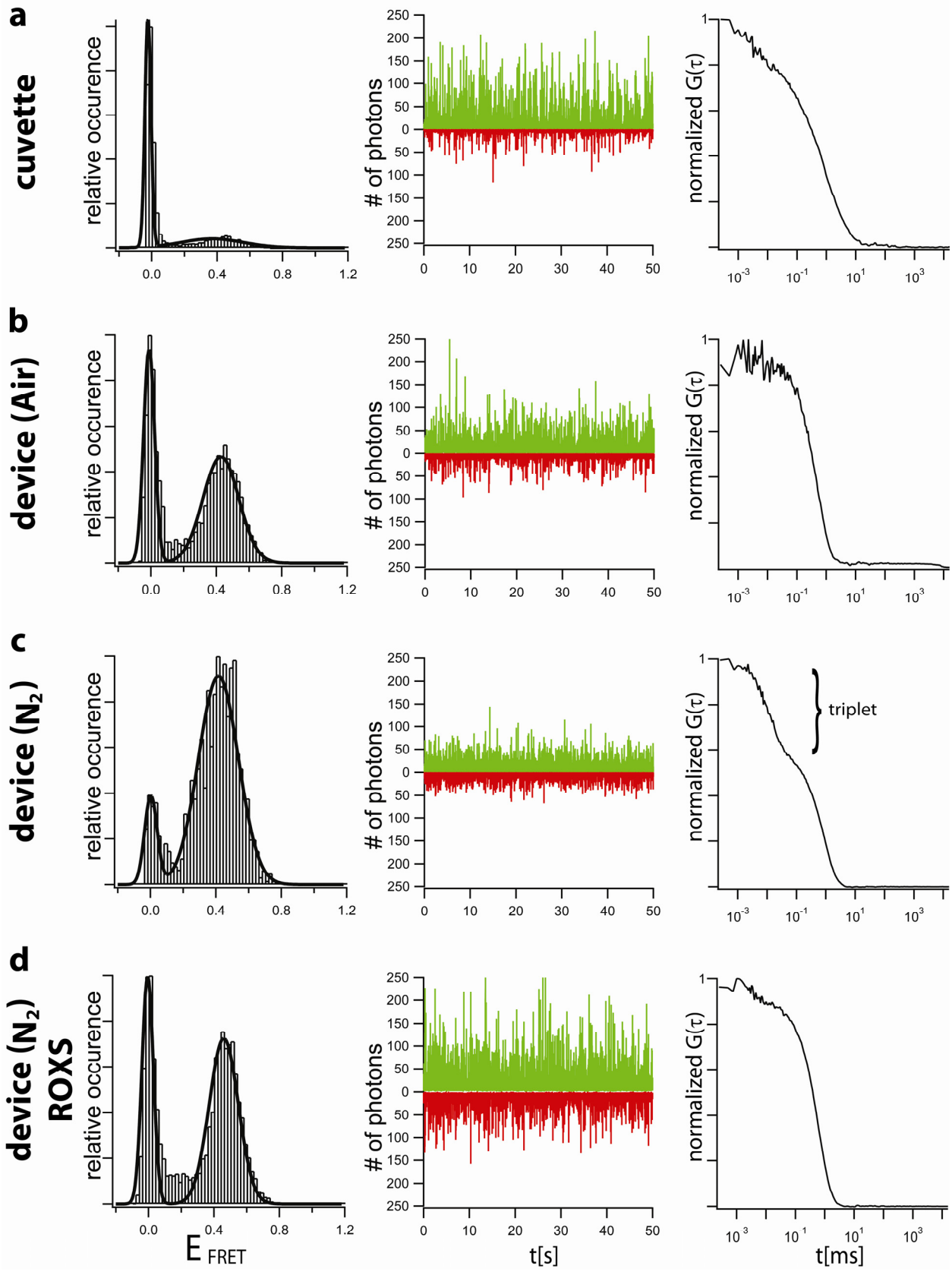
a
cuvette
b
device (Air)
c
device (N2)
d
device (N2)
ROXS
relative occurence
# of photons
normalized G(τ)
triplet
E FRET
t[s]
t[ms]

Supplementary Figure 7: Experimental data for FRET measurements of the protein T4 lysozyme dual-labeled with Alexa488 and Cy5. **(a)** Measurements under denaturing conditions (analyzed using a burst search algorithm), in a cuvette (left panel), in the device with air in the gas channels (middle panel), and with flow of N_2 through the gas channels (right panel). Similar to the experiments performed on DNA, the deoxygenation has a beneficial effect of enhancement of the ratio between the FRET peak and zero peak (right panel vs. middle panel). In addition, deoxygenation in the device make it possible to identify populations that are barely separated (right vs. middle) or even indistinguishable (right vs. left) under standard conditions. **(b)** The utility of the device for protein folding studies was also demonstrated by performing measurement on T4 lysozyme in its native conformation, after denaturant (4M GdmCl) was removed from a protein solution by diffusive buffer exchange in a laminar sheath flow. Note that due to strong surface sticking and uncontrolled sample loss under physiological conditions (0M GdmCl), the cuvette experiments were performed at 0.5M GdmCl, where the sample loss is less severe while the protein is in its folded state.[8] The microfluidic device circumvents the sticking of protein molecules to walls of the optical interrogation chamber, making it possible to test protein folding with smFRET at physiological conditions.

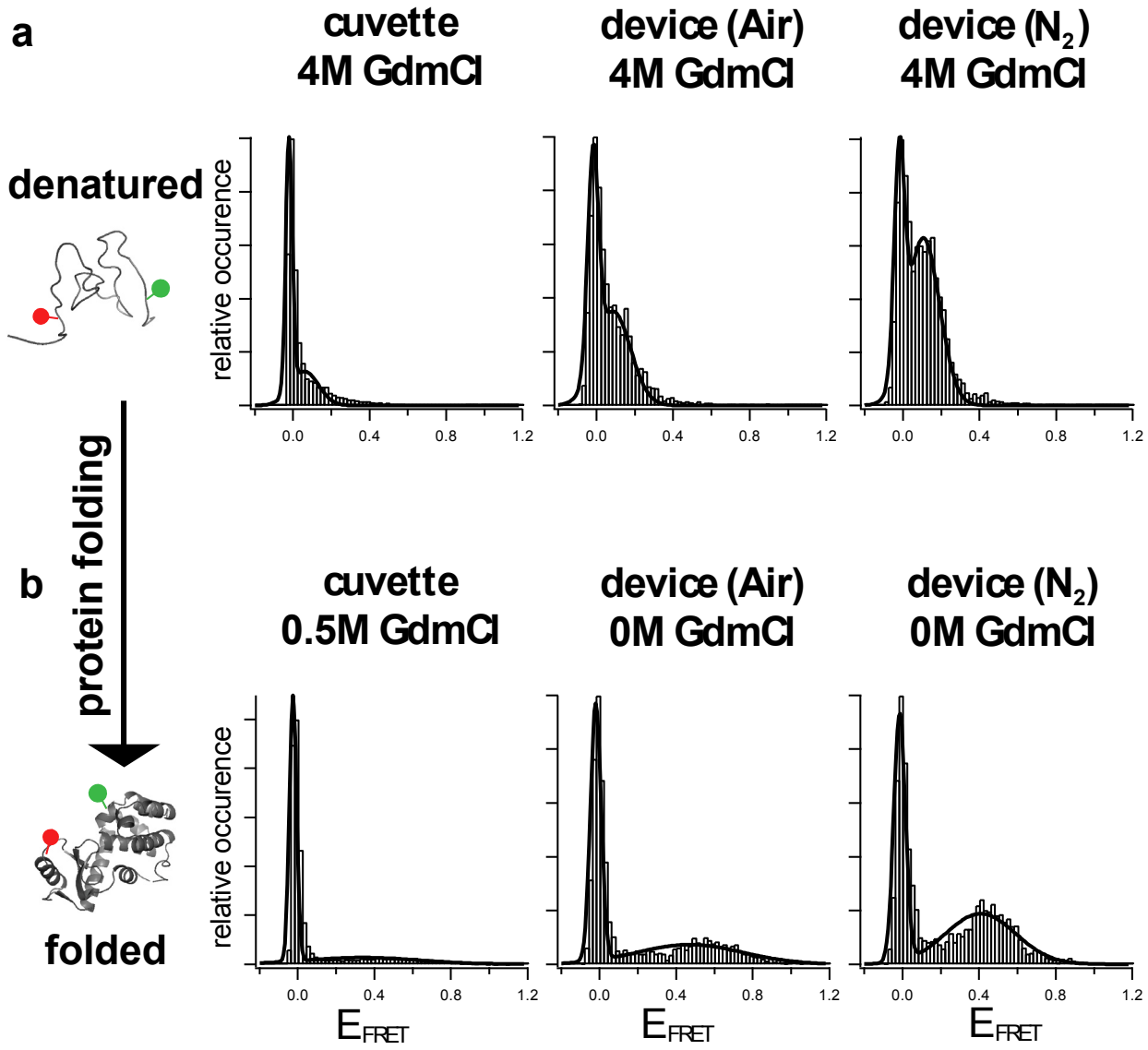

Supplementary Figure 8: Autofluorescence in the emission channel of Alexa488, in photon counts per 1 ms, for a solution of ROXS freshly prepared from methylviologen (MV) and ascorbic acid (AA) measured in a cuvette as a function of time. The increase in the autofluorescence of ROX over the course of the data (16 min) is clearly observed, in particular, in a gradual growth of the minimal number of photons counted (lower boundary of the plot). The aging of ROXS apparently results in an autofluorescent species, whose emission in the Alexa488 detection channel mimics donor only bursts. Similar autofluorescent background was observed in the microfluidic device with deoxygenation. We note that such a soluble autofluorescent species constitutes a much more serious problem in smFRET experiments on untethered molecules (using confocal detection) than on immobilized molecules (using TIRF). This autofluorescent species did not seem to interfere with our samples, but contributed to donor channel background. To minimize the autofluorescence caused by the aging of ROXS, the microfluidic device had two buffer inlets and a dedicated mixing channel, making it possible to prepare ROXS in situ from its components of AA and MV. As a result, ROXS at the measurement point always had an age of <1 min. To minimize the autofluorescence of ROXS at the measurement point, it was also important to store MV and AA solutions on ice before feeding them into the device.

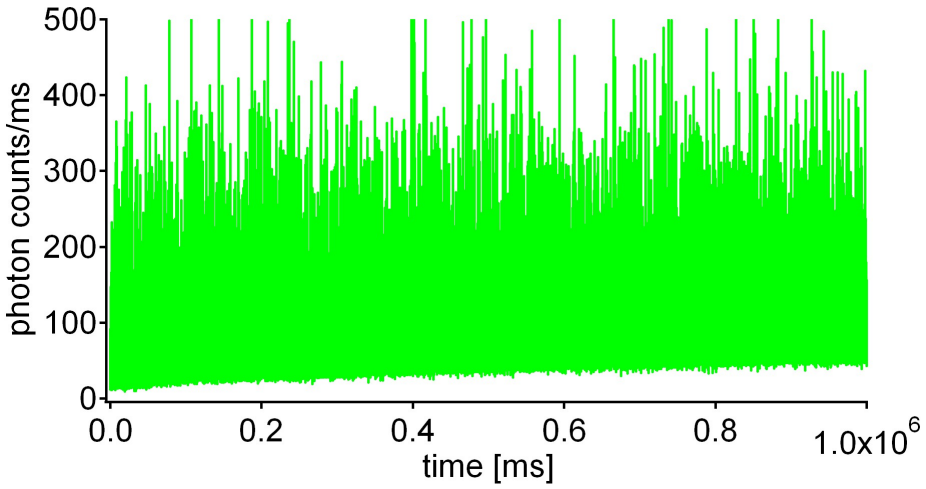

Supplementary Figure 9: Experimental data for FRET and FCS measurements of 7SK siRNA dual-labeled with Cy3b and Alexa647. siRNA against the small nuclear RNA 7SK was obtained by annealing together an Alexa647-5'-labeled antisense strand (Thermo Scientific Dharmacon, Lafayette, CO), and a sense strand 5'-labeled with Cy3b as for the DNA.[11] The experiments performed on the siRNA sample were similar to those shown in Figure 3b,c in the main text (performed on DNA dual-labeled with Alexa488-Alexa647) and included smFRET measurements in the microfluidic device with deoxygenation without the addition of ROXS (upper panel) and with the addition of ROXS (lower panel). Shown are the respective E_{FRET} histograms (fit to the N_2+ROXS peak overlaid in red), raw data time trace, and correlation curves. In the absence of ROXS, a strong triplet component in the FCS data is visible (indicated by a curly bracket). When ROXS is added, the triplet component is reduced, the brightness of the bursts increases substantially (cf. raw data time traces), and a peak at E_{FRET} ~ 0.3 becomes clearly discernible.

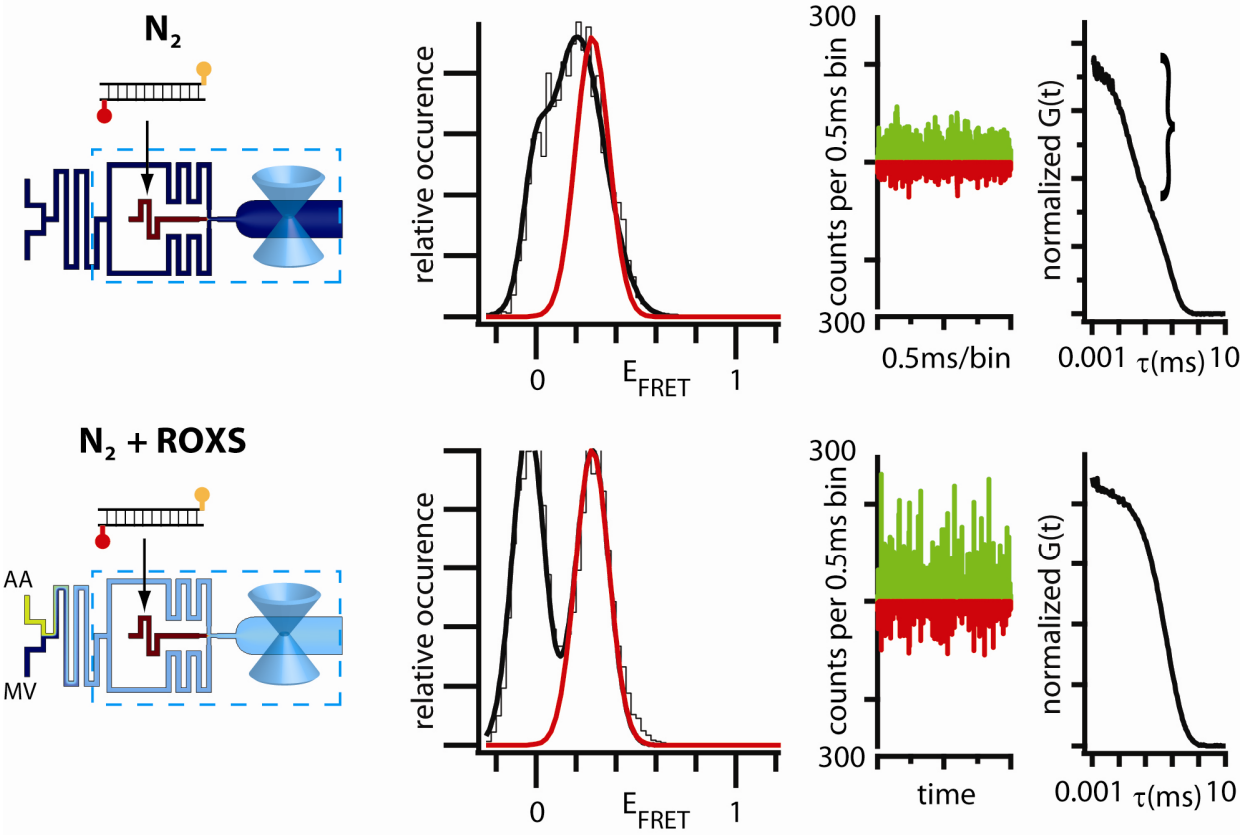

Supplementary Figure 10: Experiments in the microfluidic device with deoxygenation and addition of ROXS produce narrower FRET peaks and permit shorter integration times and faster data acquisition. The sample was the same as in Figure 3b,c of the main text. (**a**) and (**b**) display smFRET histograms with a 0.5 ms integration time. Histograms obtained in (**a**) a cuvette and (**b**) the microfluidic device with deoxygenation and addition of ROXS are shown. The data in each histogram represent 6600 individual events collected so that they had at least 30, 50, 100, or 200 photon counts (shown by curves in different colors). Substantially higher quality data obtained in the microfluidic device is evident for all four threshold values. Most notably, when the threshold was raised to 200 counts (black markers), the histogram in the device (N_2 + ROXS) still had a clear FRET peak, whereas no FRET peak could be detected in the cuvette experiment. A higher threshold results in the selection of events with better signal to noise ratio, typically producing a FRET peak with a reduced width. (**c**) FRET histogram obtained in the microfluidic device with deoxygenation and addition of ROXS with a 50 μs integration time, which was 10-fold shorter than for the rest of the FRET histograms in this study. The laser power and the flow velocity at the measurement point were, respectively, ~2.5-fold higher and 5-fold higher than in the rest of the microfluidics experiments. Even with this faster acquisition rate, the quality of the FRET peak remained high. The short integration time enabled by the microfluidic device can be used for much faster data acquisition and for the detection of hidden conformational sub-populations that convert into each other on the corresponding short time scales.

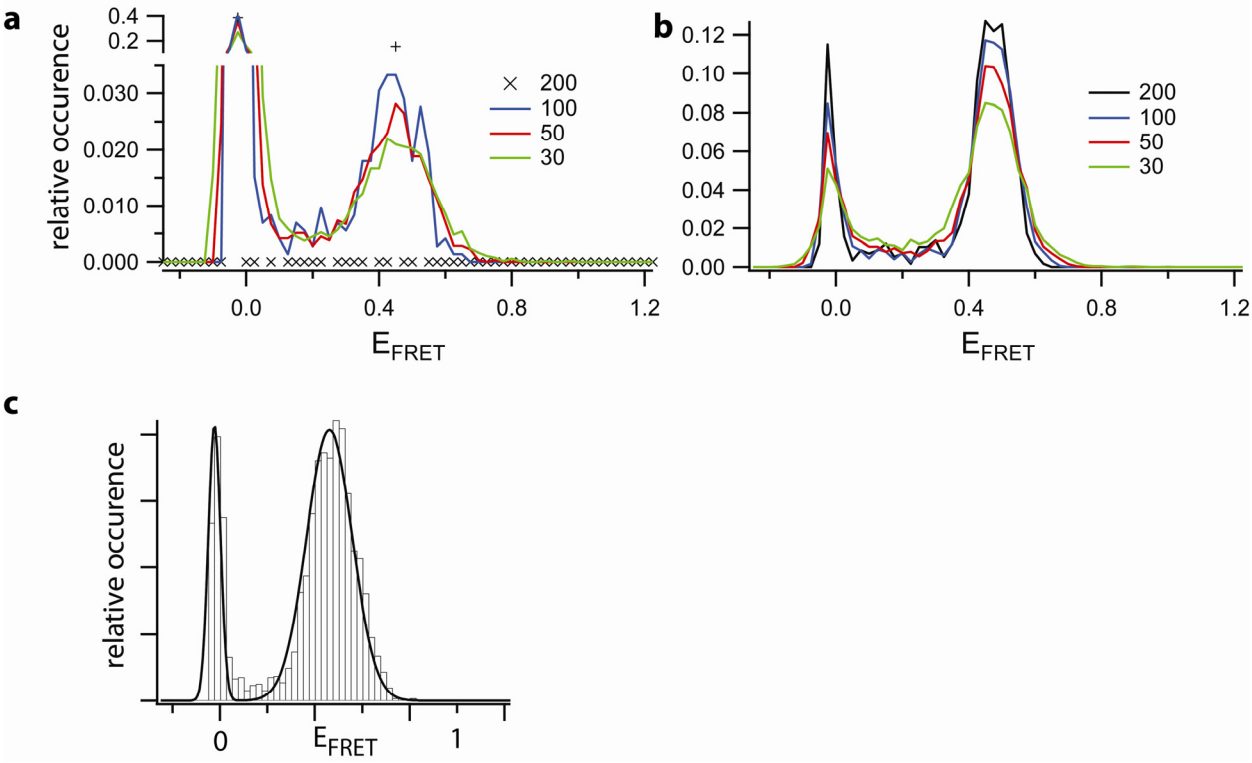

Supplementary References:

(1) Vollmer, A. P.; Probstein, R. F.; Gilbert, R.; Thorsen, T. *Lab On A Chip* **2005**, *5*, 1059-1066.
(2) Polinkovsky, M.; Gutierrez, E.; Levchenko, A.; Groisman, A. *accepted to Lab On A Chip* **2008**.
(3) Vogelsang, J.; Kasper, R.; Steinhauer, C.; Person, B.; Heilemann, M.; Sauer, M.; Tinnefeld, P. *Angewandte Chemie-International Edition* **2008**, *47*, 5465-5469.
(4) Merkel, T. C.; Bondar, V. I.; Nagai, K.; Freeman, B. D.; Pinnau, I. *Journal Of Polymer Science Part B-Polymer Physics* **2000**, *38*, 415-434.
(5) Simonnet, C.; Groisman, A. *Anal Chem* **2006**, *78*, 5653-63.
(6) Sud, D.; Mehta, G.; Mehta, K.; Linderman, J.; Takayama, S.; Mycek, M. A. *Journal Of Biomedical Optics* **2006**, *11*.
(7) Mehta, G.; Mehta, K.; Sud, D.; Song, J. W.; Bersano-Begey, T.; Futai, N.; Heo, Y. S.; Mycek, M. A.; Linderman, J. J.; Takayama, S. *Biomedical Microdevices* **2007**, *9*, 123-134.
(8) Brustad, E. M.; Lemke, E. A.; Schultz, P. G.; Deniz, A. A. *J Am Chem Soc* **2008**, *130*, 17664-5.
(9) Eggeling, C.; Berger, S.; Brand, L.; Fries, J. R.; Schaffer, J.; Volkmer, A.; Seidel, C. A. M. *Journal of Biotechnology* **2001**, *86*, 163-180.
(10) Rasnik, I.; McKinney, S. A.; Ha, T. *Nature Methods* **2006**, *3*, 891-893.
(11) Berezhna, S. Y.; Supekova, L.; Supek, F.; Schultz, P. G.; Deniz, A. A. *Proc Natl Acad Sci U S A* **2006**, *103*, 7682-7.